THE JOURNAL OF
PHYSICAL CHEMISTRY C

ARTICLE

pubs.acs.org/JPCC

Thermal Evolution of Pt-Rich FePt/Fe_3O_4 Heterodimers Studied Using X-ray Absorption Near-Edge Spectroscopy

S. J. A. Figueroa,[†] S. J. Stewart,[‡] T. Rueda,[§] A. Hernando,[§,∥] and P. de la Presa*[,§,∥]

[†]European Synchrotron Radiation Facility, 6 rue Jules Horowitz, BP 220, 38043, Grenoble Cedex, France

[‡]IFLP, CCT-La Plata, CONICET, Departamento de Física, Facultad de Cs. Exactas, Universidad Nacional de La Plata, CC 67, 1900 La Plata, Argentina

[§]Instituto de Magnetismo Aplicado, UCM-ADIF-CSIC, P.O. Box 155, 28260 Las Rozas, Spain

[∥]Departamento de Física de Materiales, Facultad de CC. Físicas, UCM, 28040 Madrid, Spain

S *Supporting Information*

ABSTRACT: FePt/Fe_3O_4 nanoparticles can be used as building blocks to obtain, upon thermal annealing, magnetic nanocomposites with combined magnetic properties. Although the pre- and postannealed samples are usually well-characterized, a detailed investigation during annealing is necessary to reveal the role of intermediate processes to produce a desirable composite. We present an alternative method using in situ XANES to investigate the thermal evolution of oleic acid- and oleylamine-coated Pt-rich FePt/Fe_3O_4 heterodimers. As the temperature increases, a progressive reduction of Fe_3O_4 to FeO occurs helped by the thermolysis of the surfactants, while above 550 K Fe_3Pt starts to be formed. At 840 K an abrupt increase of FeO further drives the phase transformation to stabilize the iron platinum soft phase. Thus, the Fe_3O_4 reduction acts as catalyst that promotes the Fe and Pt interdiffusion between the Pt-rich FePt and Fe_3O_4/FeO to form Fe_3Pt instead of exchange-coupled FePt/Fe_3O_4 with hard magnetic properties. In addition, the role of the interface of the heterodimer ends is discussed. The pre- and postannealed samples were also characterized by TEM, XRD, EXAFS, magnetometry, and Mössbauer spectroscopy.

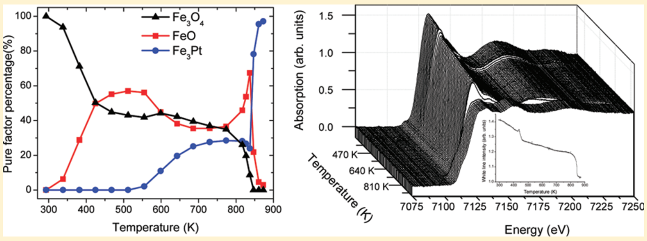

1. INTRODUCTION

Multicomponent nanostructured materials offer a series of functionalities due to their affording the possibility to retain the physical−chemical properties of single-component counterparts, thus making them attractive for specific purposes.[1] Besides, the coupling interactions between domains of coexisting materials are of relevant importance to define the multicomponent features.[2] These multifunctional nanomaterials can exhibit novel physical and chemical properties, which are essential for future technological applications if the material structure and interface coupling interactions are adequately controlled. For instance, core/shell,[3−8] yolk−shell,[9−11] and heterodimers[12−16] are well-known complex systems that have shown enhanced optical, catalytic, and magnetic properties compared to their individual single-component materials.

Among these nanomaterials, FePt-based nanocrystals attract the special attention of researchers due to their potential application in storage medium or as permanent magnets. Moreover, it has been demonstrated that, due to their low toxicity[17] and high degree of functionalization,[13,18,19] the FePt nanoparticles (NPs) are also suitable for biomedical applications, such as magnetic separation, hyperthermic ablation, and T_2 MRI contrast agents.[20−22] It is well-known that Fe_3O_4 is one of the most suitable for the latter purposes. Thus, multicomponent FePt−Fe_3O_4 NPs would be a promising material that could take advantage of the intrinsic properties of the both ends.

Recently, some efforts have been focused on synthesizing FePt-based core−shell or heterodimers to obtain soft−hard magnetic nanostructures that display exchange−spring coupling effects.[16,23−27] However, in order to obtain the FePt $L1_0$ phase with hard magnetic properties, it is usually necessary to perform a thermal annealing of the NPs, even though this may cause some disadvantages, like grain growth or coalescence. Several works have shown that the postannealed product from FePt-based core−shell or heterodimers nanocrystals depends on factors like the Fe:Pt ratio, the type of surfactant, or annealing atmosphere.[28,29] The knowledge of the kinetic process that takes place during annealing is relevant for fundamental studies but also for possible applications when a controllable magnetic response is required. Thus, a detailed investigation of the thermal evolution of FePt-based bicomponent samples is still necessary to obtain valuable information on the role of intermediate phases and transformations involved during the annealing.

Received: December 6, 2010
Revised: February 11, 2011
Published: March 07, 2011

To this aim, here we investigate the thermal evolution of FePt-based metallic/magnetic nanocrystal prepared by a one-pot, one-step chemical synthesis method. We study their magnetic properties and investigate the stability of the as-made nanocrystal having a noncentric geometry. Our investigation is focused on the thermal evolution of heterodimers during the annealing under an inert atmosphere. The thermal evolution was followed by in situ time-resolved Pt L_3 and Fe K edges X-ray absorption near-edge spectroscopy (XANES) experiments. Throughout the semiquantitative analysis of XANES spectra we are able to follow the evolution of the phases involved during the annealing. The sample characterization is also complemented by using X-ray diffraction (XRD), transmission electron microscopy (TEM), extended X-ray absorption fine structure (EXAFS), Mössbauer spectroscopy, and magnetometry. Our results demonstrate the important role played by the different reduction processes that take place during the heat treatment. This fact as well as the effect of the absence of a surfactant interface between heterodimers' domains is discussed to explain the stabilization of a soft magnetic phase. We believe that this fundamental study give a pathway to obtain exchange-coupled materials with tunable properties, i.e., through the control of reducing mechanisms and interface influence.

2. EXPERIMENTAL METHODS

2.1. Synthesis. The NPs have been synthesized by a high-boiling coordinating solvent method.[13] The procedure involved heating 0.5 mmol of platinum(II) acetylacetonate [Pt(acac)$_2$] (Sigma-Aldrich, 99.99%) in 15 mL of 1-octadecen (Alfa Aesar, tech 90%) under N_2 flux up to 120 °C, followed by the injection of 2.5 mmol of oleic acid (Sigma Aldrich, tech. 90%) and oleyamine (Sigma Aldrich, tech 70%) and 3 mmol of iron pentacarbonyl [Fe(CO)$_5$] (Sigma Aldrich). The balloon flask was then sealed to avoid oxidation and kept under a blanket of nitrogen. The solution was slowly heated at a rate of 5 K/min up to 320 °C and refluxed for 30 min. Afterward, the black dispersion was cooled down to room temperature (rt). The obtained NPs were cleaned by cyclic precipitation and redispersed with ethanol (Panreac, absolute PRS) and hexane (Alfa Aesar, HPLC grad 95%). Finally, the particles were stored in 25 mL of hexane with 0.05 mL of oleic acid and oleylamine in a glove chamber.

The concentration of iron and platinum atoms was determined with elemental analysis. For this purpose samples were digested with HNO_3 to oxidize the organic coating and then with HCl to dissolve the metals. The Fe:Pt concentration was then measured in an induced coupled plasma emission spectrometer (ICP-ES) (Perkin Elmer Optima 2100 DV). The result gives a Fe:Pt mean composition of 67:33.

The as-synthesized NPs were thermally treated under inert atmosphere up to 873 K for different experiments (see below).

2.2. XRD and TEM Characterization. Phases, crystal parameters, and grain size were determined by rt XRD measurements, which were carried out with a Siemens diffractometer D5000, using Cu Kα radiation. The particle sizes were characterized by TEM micrographs in a 200 keV JEOL-2000 FXII microscope. A drop of the dispersed suspension was placed onto a copper grid covered by a carbon film. The mean particle size, d, and the logarithmic standard deviation, σ, were obtained from digitized TEM images by counting more than 200 particles. Because the NPs are not spherical, the maximum Feret's diameter was used to compute the size, i.e., the maximum perpendicular distance between parallel lines which are tangent to the perimeter at opposite sides.

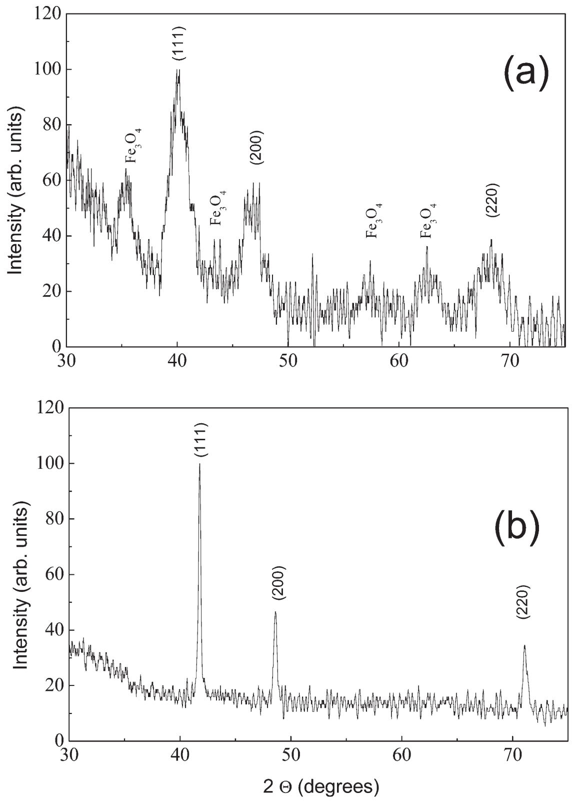

Figure 1. X-ray diffraction pattern of as-made heterodimers (a) and after annealing at 873 K in inert atmosphere (b).

2.3. X-ray Absorption Experiments. The experiments were performed in the multibunch mode at the D04B-XAFS-1 beamline of the Laboratório Nacional de Luz Síncrotron (LNLS), Campinas, Brazil. To take the absorption spectra, a few drops of the dispersed suspension was placed onto a boron nitride pellet. All spectra were collected at rt in transmission mode using a channel cut monochromator [Si(111)]. Three gas-filled ionization chambers were used in series to measure the intensities of the incident beam, the transmitted beam through the sample, and the beam transmitted by a reference foil in order to calibrate accurately the energy. The primary vertical slit size was about 0.3 mm, and this yielded a resolution of about 2.0 eV on Fe K edge and close to 6.8 eV on Pt L_3 edge. The EXAFS signal $\chi(k)$ was extracted using Athena and analyzed using the Arthemis software package. Simultaneous EXAFS fits of samples and references were performed (for details, see Supporting Information, section 1). Pre-edge XANES fits at the Fe K edge were performed following the procedure described by Wilke et al.[30]

In situ XANES spectra at Fe K and Pt L_3 edges were collected in transmission mode using the D06A-DXAS beamline at LNLS.[31] The XANES experiment was performed in a controlled-atmosphere cell heating the sample at a rate of 3 K/min in a flow of inert atmosphere (He) from ambient temperature up to 873 K and collecting synchronously mass spectrometry (GSD 301 Omnistar) data of the exhaust. The XANES data analysis was performed by subtracting a linear background and rescaling the absorbance by normalizing the difference between the baseline and the postedge absorption in a region approximately 300 eV behind the edge. Factor analysis (FA) was performed by using the FACTOR program.[32−35]

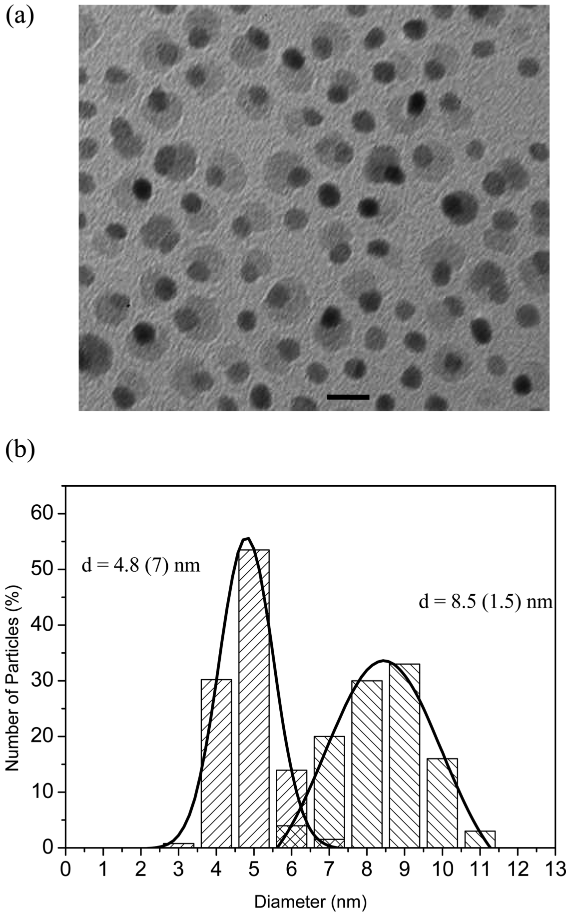

Figure 2. (a) TEM micrograph of as-made heterodimers; the scale bar is 10 nm. (b) Size distribution of the heterodimer head and body.

2.4. Mössbauer and Magnetic Characterization.

The as-made and thermally treated samples were characterized magnetically by means of Quantum Design SQUID and vibrating sample magnetometer. Hysteresis loops were taken at 10 and 300 K and at a maximum applied field of 5 T. The thermal behavior was determined by zero-field-cooled (ZFC) and field-cooled (FC) measurements at a 100 Oe applied field. For these measurements, the as-made NPs solution was dried under an inert argon atmosphere and weighted.

^{57}Fe Mössbauer spectra at 300 and 30 K were recorded in transmission geometry with a 512-channel constant acceleration spectrometer and a source of ^{57}Co in Rh matrix of nominally 25 mCi. Isomer shifts (IS) are referred to metallic α-Fe at rt. The 30 K temperature was achieved using a Displex DE-202 closed cycle cryogenic system. Mössbauer spectra were fitted using the Recoil software package.[36]

3. RESULTS AND DISCUSSION

3.1. As-made NPs.

The XRD pattern (Figure 1) shows the Bragg reflections belonging to an iron oxide with cubic structure in addition to those of an fcc metal compound (Pt) with a cell parameter a = 3.92 Å. The grain size calculated using the Scherrer's equation is 5 ± 1 nm for the metal compound and 7 ± 1 nm for the oxide.

Figure 2a shows a representative TEM micrograph of the as-made NPs. The particles are heterodimers with a nonsymmetric snowmanlike shape, showing a large body and a small head, the latter exhibiting a comparatively darker image contrast. The dark region corresponds to a higher electron density, likely associated with the metallic component, whereas the lighter one might be related to the presence of the oxide phase.[13,16] Figure 2b shows the estimated mean particle size d and standard deviation σ for both the heterodimer head and body. By counting more than 200 NPs, the average values are d = 4.8 nm and σ = 0.7 nm for the head, and d = 8.5 nm and σ = 1.5 nm for the body. These values agree well with those determined by XRD. The smaller size obtained from XRD can be due to atoms at the particle surface that do not diffract coherently.

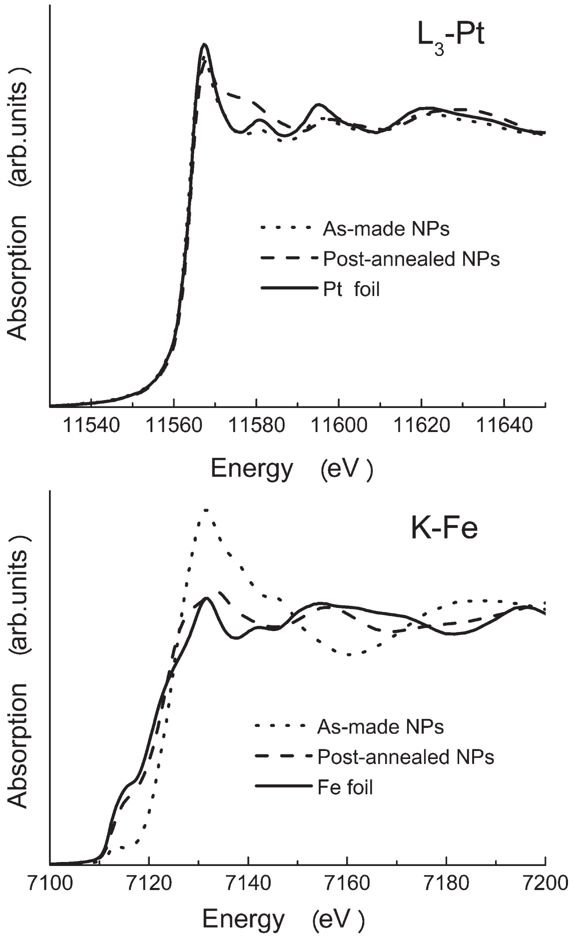

Figure 3. XANES spectra at the Pt L_3 and Fe K edges of as-made Pt-rich FePt/Fe_3O NPs. Spectra of Fe and Pt reference foils are also shown for comparison.

Figure 3 shows the Fe K edge and Pt L_3 XANES spectra of as-made NPs. XANES features at the Fe K edge mainly resemble those corresponding to magnetite Fe_3O_4. The pre-edge energy position is compatible with a $Fe^{3+}-Fe^{2+}$ mixture.[30] The main component of the pre-edge peaks of Fe_3O_4 arises from tetrahedrally coordinated Fe^{3+}, and the shoulder corresponds to $Fe^{2+}-Fe^{3+}$ ions octahedrally coordinated. The average oxidation state of iron from these XANES data is 2.5(1)+, which is slightly less than expected for Fe_3O_4 (2.67+). This value indicates that the major iron phase is magnetite, but the sample might contain a small percentage of a metallic phase (see below). From this result the amount of the other spinel iron phase maghemite γ-Fe_2O_3 regularly found in iron oxide NPs, if any, is quite low.[37]

Table 1. EXAFS Fe K and Pt L_3 Edge Fitted Parameters of Pt-Rich FePt/Fe_3O_4 Heterodimers[a]

sample	edge	shell[b]	N	R (Å)	σ^2 (Å^2) × 10^{-2}	E_0 (eV)
as-made NPs	K Fe	$O_{Fe_3O_4}$	4.1 ± 0.2	1.890 ± 0.007	4.3 ± 0.7	−7.2 ± 1.3
		$O_{Fe_3O_4}$	6.3 ± 0.2	2.020 ± 0.006	5.2 ± 0.7	−7.2 ± 1.3
	L_3 Pt	$Pt_{(1-x)\ Pt}$[c]	9.4 ± 1.2	2.744 ± 0.005	0.64 ± 0.08	6.6 ± 1.2
		$Fe_{x\ Pt}$[c]	9.4 ± 1.2	2.744 ± 0.005	0.64 ± 0.08	6.6 ± 1.2

[a] N is the coordination number, R is the average distance to the central atom, σ^2 is the Debye−Waller factor, and E_0 is the energy shift. [b] Model compound used to obtain the phases. [c] The value obtained for the iron dopant is $x = 0.10 \pm 0.05$.

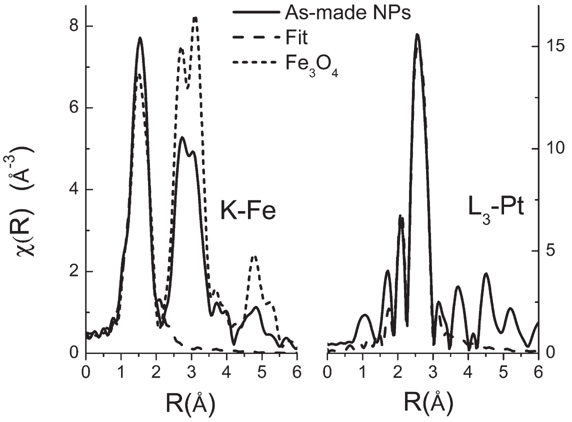

Figure 4. Fourier transforms of $k^3\chi(k)$ EXAFS at Pt L_3 edge and at Fe K edge of the as-made Pt-rich FePt/Fe_3O_4 NPs. Solid lines correspond to the fitting results with parameters shown in Table 1. XANES of bulk Fe_3O_4 is also shown for comparison.

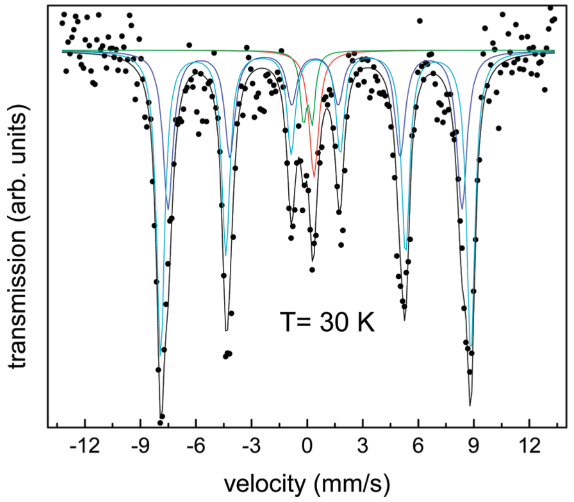

Figure 5. Mössbauer spectra at 30 K of the as-made Pt-rich FePt/Fe_3O_4 NPs.

Fe K edge EXAFS are acceptably fitted to a cubic spinel structure (see Table 1). The Fe−O distances are close to the values of 1.89 and 2.06 Å expected for the tetrahedral and octahedral sites in Fe_3O_4, respectively. A reduction of the amplitude of the second main peak is observed when compared with the Fourier transform of bulk Fe_3O_4, which is probably related to the local structural disorder due to the higher percentage of atoms at the particle surface layer in as-made NPs.

We observe that Pt L_3 edge XANES of the as-made NPs and Pt reference foil are similar, suggesting that the Pt local structure mainly resembles that corresponding to Pt metal rather than to a FePt alloy.[38] A more detailed analysis can be extracted from the Fourier transforms $\chi(R)$ of the EXAFS spectra at the Pt L_3 edge shown in Figure 4 (fitting results are shown in Table 1). The nearest neighbor distance Pt−Pt (or Pt−Fe) is close to 2.74 Å, which is shorter than the value expected for pure platinum (2.77 Å). This would indicate the incorporation of low quantity (*circa* 10 at.%) of iron into platinum forming a FePt alloy. This is also supported by the presence of a small phase shift on $\chi(k)$ signals (see Supporting Information, section 2). Hereafter we will refer to this component as the Pt-rich FePt head of the heterodimer. Reports on equiatomic FePt NPs with a Pt-rich core and Pt-depleted shell can often be found in the literature.[38−41] The explanation of the inhomogeneity in the Pt concentration lies in the different nucleation velocity of both atomic species: Pt atoms nucleate faster than the Fe ones, leading to a Pt concentration that decreases from inside to outside of the NP.

The Mössbauer spectrum of the as-made NPs showed an absorption signal only below the fusion temperature of oleic acid T_f = 281 K. The spectrum taken at 250 K (not shown) mainly consisted of a broad doublet signal. At 30 K the spectrum (Figure 5) shows a resolved magnetic signal (relative area percentage about 90%) plus a nonmagnetic or relaxing signal with IS = 0.37 mm/s that represents unblocked iron oxide particles. A small doublet with a relative area approximately 5% was also included (IS = 0.03 mm/s), which can be assigned to a metallic minority phase. The magnetic signal needs to be fitted with at least two sextets, but the lack of resolution due to the broad lines and the poor signal/noise ratio makes the determination of proportions and parameters of each component difficult. The best fit was obtained assuming one sextet with hyperfine field B_{hf} = 519 kOe and IS = 0.48 mms, and another one with B_{hf} = 491 kOe and IS = 0.42 mm/s. Both sextets are assigned to blocked Fe_3O_4 NPs, but γ-Fe_2O_3 cannot be ruled out.[42,43] Further, these results indicate that, within the Mössbauer window time, the heterodimer's body composed of iron oxide behaves superparamagnetically at ambient temperature.

A quite common difficulty found in several investigations about nanosized iron oxides is related with the distinction between Fe_3O_4 and γ-Fe_2O_3, either whether these oxides are the only components[37,44] or when they are chemically bounded to other materials.[45] Indeed, both oxides have the same spinel structure and similar saturation magnetization, the latter being affected by size and/or surface effects.[46] Also, the Mössbauer hyperfine parameters are modified with respect to those belonging to their bulk counterparts, and the contribution of each oxide can only be estimated by taking spectra under an applied magnetic field.[47] In our case, even though the Mössbauer and XRD results are not conclusive, the oxidation state determined by XANES and EXAFS results suggest that the oxide part consists of Fe_3O_4.

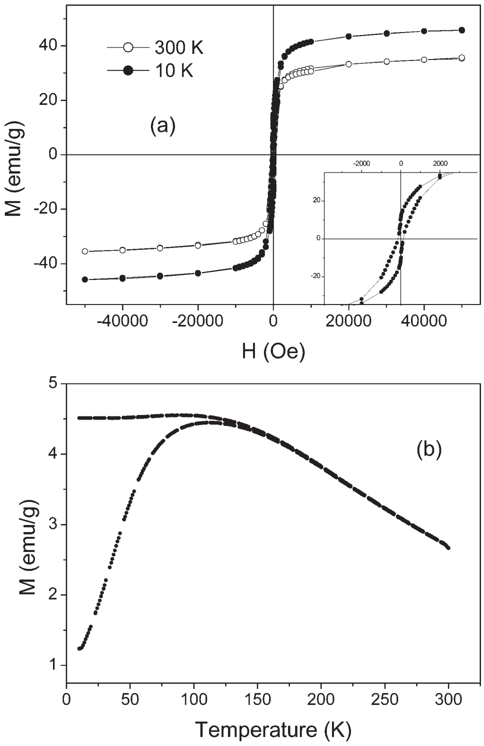

Figure 6. (a) M vs H at 5 and 300 K. The inset shows a detail of the hysteresis curve at 10 K. (b) M vs T curves of as-made heterodimers NPs; the applied field is 100 Oe.

The magnetic saturation (M_S) at 10 K is 30 emu/g_{NP} (per gram of NP), whereas at ambient temperature the saturation is about 20 emu/g_{NP} (see Figure 6). Considering the average composition of as-made heterodimers ($Fe_{67}Pt_{33}$), M_S per gram of Fe_3O_4 can be roughly estimated as 68 emu/g_{oxide}. This M_S value is lower than the M_S of bulk Fe_3O_4 (90 emu/g) and can be ascribed to the spin disorder at the surface of the NPs. The room temperature $M-H$ loop shows small hysteresis (coercitive field H_C = 10 Oe), increasing at 10 K to H_C = 150 Oe. The departure of the FC magnetization curve from the ZFC one, characteristic of the presence of moments getting blocked, occurs at about 130 K (Figure 6). The blocking temperature (T_B) corresponding to the maximum of the ZFC curve is about 110 K. The broad ZFC maximum (Figure 6) suggests that there are strong magnetic dipole—dipole and/or exchange interactions among the particles. Thus, our results indicate that the as-made NPs consist of a heterogeneous distribution of atoms forming a metallic oxide Pt-rich FePt/Fe_3O_4 heterodimer.

It is important to highlight that our synthesis procedure consists of adding the platinum salt and the iron pentacarbonyl to the solution in one step at the beginning of the synthesis. This route slightly differs from others previously reported,[13,16,23] in which first FePt seeds or NPs are formed and afterward more iron pentacarbonyl or iron oxide NPs are added to get bimagnetic FePt—iron oxide NPs. We believe that in our case, due to the fact that Pt atoms nucleate faster than the Fe ones, the nucleation of FePt NPs takes place during the initial stages of the reaction. Once the Pt is exhausted, the remaining iron atoms grow on a surface defect of FePt, giving a place for the iron oxide body of the heterodimer. The fact that the oxidized body consist of Fe_3O_4 would indicate that the thermal decomposition of organic precursors in 1-octadecene solvent operates to stabilize magnetite.[46] In addition, the storage in an inert atmosphere to avoid exposure to air has prevented the heterodimers from oxidizing. Recently, Corrias et al.[37] demonstrated that the smaller the sizes of iron oxide NPs the component Fe_3O_4 becomes more stable; i.e., the risk of oxidation decreases.

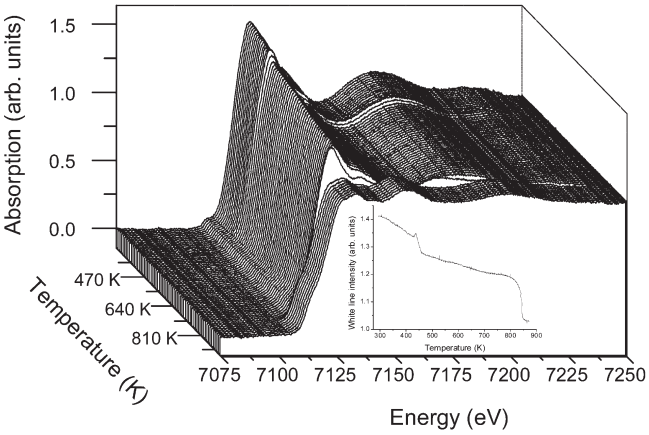

Figure 7. XANES spectra at Fe K edge in thermal evolution treatment in He atmosphere of Pt-rich FePt/Fe_3O_4 heterodimers. The inset shows the white line evolution along the treatment.

Summarizing, our NPs can be visualized as two different entities attached to each other but without border (like conjoined twins). Apart from differences in size and shape, the morphology of these NPs differs from that previously reported,[16,23] where NPs are composed of two different entities, probably attached by the surfactant, but with a well-defined frontier or boundary.

3.2. Thermal Evolution of Pt-Rich FePt/Fe_3O_4 Heterodimers. To follow the thermal evolution of these Pt-rich FePt/Fe_3O_4 heterodimers, we have performed in situ XANES experiments at Pt L_3 and Fe K edges. We observed that the Fe K absorption edge position (see Figure 7) shifts monotonically toward lower energy values along the treatment, indicating a progressive reduction of Fe-containing phases. The Fe K edge intensity of the white line (W-L) centralized at about 7130 eV progressively decreases as the annealing temperature increases, showing a relative maximum near 440 K (see inset Figure 7). In addition, an abrupt intensity decrease of W-L occurs at about 840 K. These changes are concomitant with the maximum values of H_2 and CO detected by mass spectrometry (see Supporting Information, section 4). A similar behavior at the same temperatures was observed for the intensity of the W-L line corresponding to the Pt L_3 edge that corresponds to the electron transition from core 2p electrons to unoccupied 5d states (not shown). A decrease of the W-L could be either due to lower Pt 5d vacancies or to size effects.[48,49]

To further characterize the thermal evolution of FePt/Fe_3O_4 heterodimers, a set of Fe K edge XANES spectra has been subjected to factor analysis (FA). The hypothesis behind FA is that a large data set (**D**) consists of a linear combination of a limited number of n factors. Thus, the large data set containing r spectra each having c data points can be reproduced by two matrices, one of them (**S**) containing the basic spectral factors and the other one (**C**) containing the corresponding concentration profile of the factors in each of the original spectra, with **E** representing the residual or error matrix,

$$\mathbf{D}_{r\times c} = \mathbf{C}_{r\times n}\cdot\mathbf{S}_{n\times c} + \mathbf{E}_{r\times c}$$

The goal is the determination of the number n of factors (or components) in the data set which corresponds to the rank of

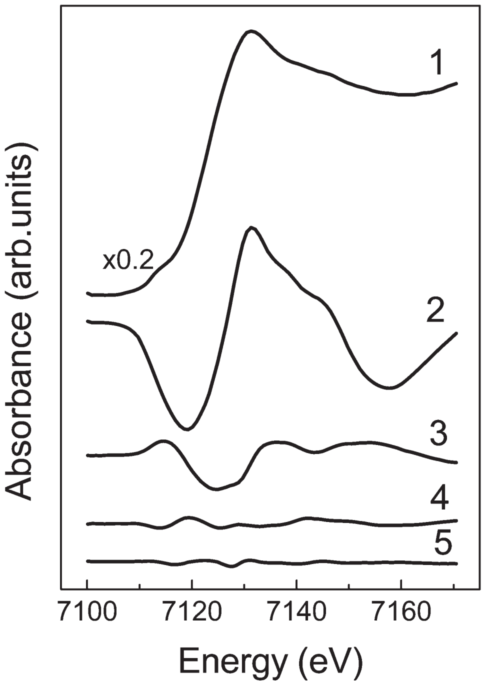

Figure 8. Abstract spectral factors.

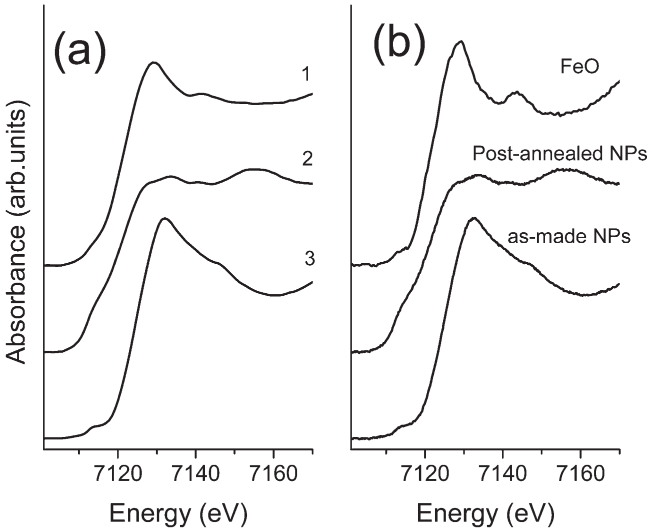

Figure 9. (a) Predicted pure components for FePt sample at the Fe K edge. (b) Experimental XANES of iron phases to be compared with the predicted components along the treatment (component 1, FeO; component 2, as made NPs; component 3, postannealed sample).

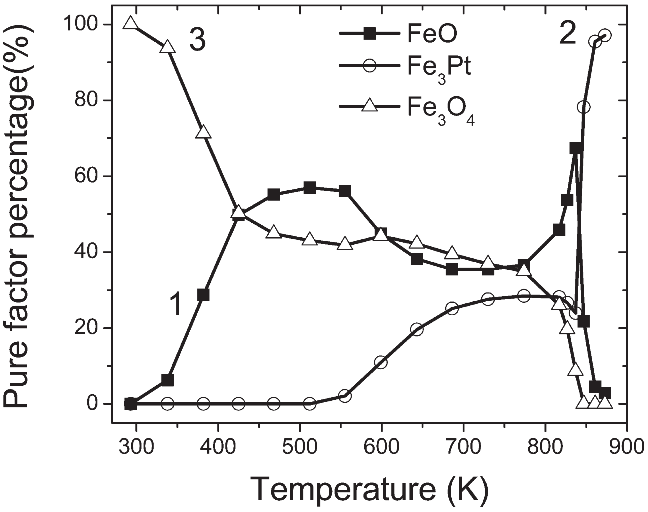

Figure 10. Thermal dependence of the percentage of iron species Fe_3O_4, FeO, and Fe_3Pt obtained by performing a factor analysis (FA) of the Fe K edge XANES data.

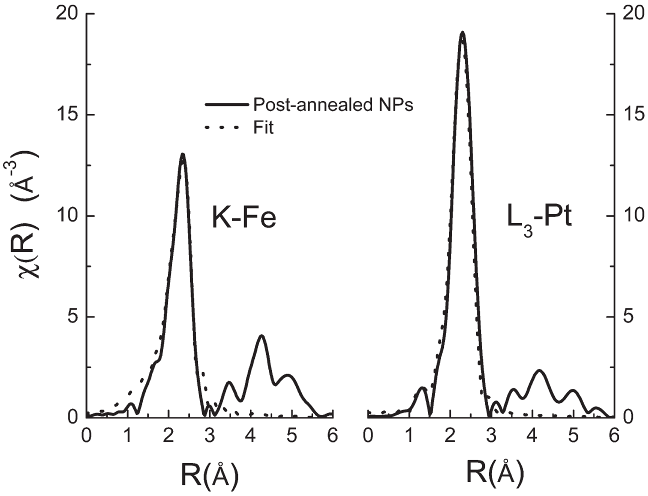

Figure 11. Fourier transforms of $k^3\chi(k)$ EXAFS data after treatment at the Pt L_3 edge and Fe K edge.

the data matrix used in the analysis. Therefore, evolving factor analysis (EFA)[50] was used to determine that the number of factors can be fixed to three. Details of this analysis can be found in the section 3 of the Supporting Information.

Figure 8 shows the abstract row matrix (spectral factors), with the first five columns represented, giving visual evidence that the abstract factors number one, two, and three are the main signals. Fourth and fifth abstract factors are dominated by low-frequency background errors. Once the number of factors is established, the abstract **C** and **S** matrices can be obtained. Their adequate rotation by the iterative transformation factor analysis (ITTFA) gives the final solution, which is represented in Figure 9(a) ($\mathbf{C}_{r\times n}$ matrix) and Figure 10 ($\mathbf{S}_{n\times c}$ matrix).

Figure 9a shows the three spectral components determined by FA, while Figure 9b shows XANES taken under the same experimental conditions to tentatively identify these components. Spectra 2 and 3 can be clearly linked to initial and final iron species, i.e., as-made Pt-rich FePt/Fe_3O_4 heterodimers and Fe_3Pt (see discussion below), respectively, assumed as the single phases at these stages. Even though the assignment of spectrum 1 is not straightforward, a simple inspection allowed us to qualitatively establish that their spectral factor has similar features with XANES of iron oxide FeO (wüstite) (Figure 9). Figure 10 shows the result of FA by considering some selected spectra. At the first stages, the percentage of Fe_3O_4 decreases at the expense of component 1. Above 550 K, the Fe_3Pt phase starts to be formed at the consequent detriment of the iron oxide phases. We observe that the percentage of component 1 displays an abrupt peak at about 843 K, coincidently with a

Table 2. EXAFS Fe K and Pt L_3 edge fitted parameters of Pt-rich FePt/Fe_3O_4 heterodimers (postannealed NPs). [a]

sample	edge	shell[b]	N	R (Å)	σ^2 (Å^2) × 10^{-2}	E_0 (eV)
postannelled NPs	K Fe	O_{FeO}	5.4 ± 1.5	1.97 ± 0.11	4.5 ± 3.2	6.7 ± 4.2
		Pt_{Fe_3Pt}[c]	3.6 ± 1.5	2.59 ± 0.01	0.9 ± 0.1	6.7 ± 4.2
		Fe_{Fe_3Pt}[c]	7.2 ± 1.5	2.59 ± 0.01	1.2 ± 0.1	6.7 ± 4.2
	L_3 Pt	Pt_{Fe_3Pt}[c]	10.8 ± 1.5	2.59 ± 0.01	11 ± 0.8	4.6 ± 4.7

[a] N is the coordination number, R is the average distance to the central atom, σ_2 is the Debye−Waller factor, and E_0 is the energy shift. [b] Model compound used to obtain the phases. [c] A third cumulant was used to fit all these shells. Values obtained were $-4 \pm 2 \times 10^{-4}$.

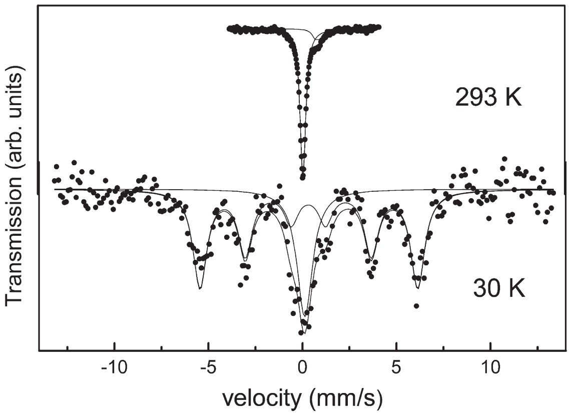

Figure 12. Mössbauer spectra of postannealed NPs recorded at 293 and 30 K. Solid lines correspond to fitting results.

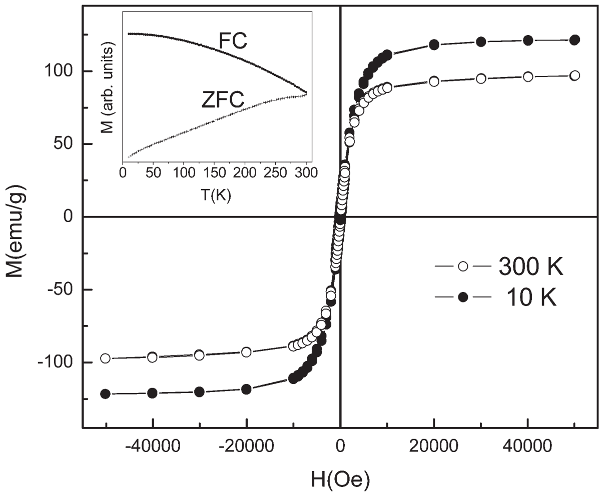

Figure 13. M vs H of postannealed NPs measured at 10 and 300 K .

marked W-L detriment (see Figure 7). This temperature is around the eutectic point where FeO−Fe_3O_4 and Fe coexist, and a temperature increase strongly favors the reduction of FeO to a metallic phase.[51] This behavior reinforces our assumption that this component 1 would represent the formation of wüstite as an intermediate phase in the reduction process that takes place during the thermal annealing.

It is well-known that fcc FePt NPs transform to the hard magnetic phase above 820 K.[52] Therefore, the fact that Fe_3Pt begins to nucleate at 550 K suggests that the energy of formation of Fe_3Pt from Pt-rich FePt/Fe_3O_4 heterodimers is lower than the energy needed to transform FePt NPs from cubic to tetragonal symmetry.

3.3. Heterodimers Postannealing: Fe_3Pt Stabilization. XRD reflections of the annealed heterodimers can be indexed to an Fe_3Pt intermetallic compound with a Cu_3Au-type structure ($L1_2$) with a cell parameter a = 3.74 Å.[53] The narrowing of XRD peaks with respect to the as-made sample shows the improvement of the crystallinity. The average grain size estimated by using the Scherrer's equation is 80 nm.

The Fe K edge XANES spectrum showed a metallic pre-edge feature (Figure 3). Both, the W-L and postedge region features resemble those of ordered Fe_3Pt.[54] Simultaneous fits results of Fourier transform of EXAFS signals at Pt L_3 and Fe K edges without phase correction (Figure 11, Table 2) indicate that the Pt and Fe environments coincide with those expected for Pt and Fe in the Fe_3Pt compound.[55]

The rt Mössbauer spectrum can be decomposed into a central singlet (IS = 0.08 mm/s, relative area 0.9) and a weak Fe^{2+} signal (IS = 0.87 mm/s), the latter probably related to the residual FeO also indicated by FA. The spectrum taken at 30 K mainly shows a broad magnetic contribution with B_{hf} = 362 kOe and IS = 0.33 mm/s, which we assign to iron at Fe_3Pt sites (Figure 12).[56] The difference between FC and ZFC magnetization curves starts above rt and increases monotonically when lowering the temperature (see inset Figure 13). The ZFC maximum occurs at a temperature above ambient. The M−H curve measured at 298 K presents hysteresis with H_C = 75 Oe, while at T = 10 K, H_C = 185 Oe. M_S at 10 K was found to be about 120 emu/g_{NP}, this value being close to the magnetic moment reported for Fe_3Pt.[53]

The present results show that the reduction of the iron oxide phase plays an important role that favors the interdiffusion of Pt and Fe atoms. This statement might be explained as follow. Heat treatment in an inert atmosphere leads to the surfactant decomposition that releases C, CO, and H_2, producing a stark reducing atmosphere (see Figure 6 in section 4 of the Supporting Information). A first process, that takes place from rt to about 550 K, is the progressive reduction of Fe_3O_4, which transforms to FeO (see Figure 10). Above this temperature, the release of more hydrogen and hydrocarbons further reduces Fe^{2+} and Fe^{3+} to Fe^0 to give rise to the Fe_3Pt phase. The latter implies that Fe and Pt interdiffusion has started to take place. Up to about 725 K, the amount of Fe_3Pt increases at the expense of further reduction of magnetite and wüstite and the resulting interdiffusion. By increasing the annealing temperature, Fe_3O_4 continuously transforms to FeO, whereas the amount of the metallic component remains almost constant. The Fe_3O_4 to FeO transformation reaches a maximum near 840 K, a temperature close to the eutectic point, where FeO−Fe_3O_4 and Fe coexist. Afterward, the remaining Fe^{2+} reduces to Fe^0 and the interdiffusion is once more activated. Thus, as the annealing temperature reaches 840 K, the nucleated intermetallic phase further drives the complete transformation and frustrates the formation of a hard−soft nanocomposite.

The interdiffusion process is probably helped by the fact that the coexisting domains are continuously attached. Another mechanism would take place when FePt and Fe oxide NPs are bounded only by surfactants, i.e., there exists physical frontiers between the particles.[16,23,57] In these cases, the Pt atoms would need to overcome the energy barrier of the interface FePt/Fe oxide to form Fe_3Pt. As the thermal energy is lower than the interface energy barrier, the Pt atoms would be limited to spread out in the same FePt NP, favoring the phase transformation of FePt from cubic to tetragonal structure. Once the thermal energy matches the interface energy barrier, the Pt atoms are free to move to the iron oxide NPs to finally form Fe_3Pt. This assumption about the function of the frontiers of the heterodimers' ends needs to be confirmed by performing new experiments.

4. SUMMARY AND CONCLUSIONS

Surfactant-coated iron platinum NPs with molar ratio 67:33 were synthesized by a wet chemical one-pot, one-step method, giving rise to a heterogeneous distribution of atoms that forms a metallic oxide Pt-rich FePt/Fe_3O_4 heterodimer, which behaves superparamagnetically at rt. Due to the synthesis procedure, both ends of the heterodimer are attached to each other without borders.

As-made NPs were subjected to thermal annealing under an inert gas flow and their evolution was followed by means of in situ XANES experiments. Results from FA analysis of these spectra showed the progressive reduction of the sample. During the first stages, a progressive reduction of the type $Fe_3O_4 \rightarrow 3FeO + O$ of the heterodimers' body takes place. The metallic part showed an increase of the *d*-electron density of Pt atoms. The presence of reducing agents, such as C, CO, and H_2 released from the thermolysis of oleic acid and oleylamine might contribute to produce changes in the oxidation state of the heterodimers. At about 440 K, the iron oxide reduction produces a relatively high percentage of FeO. Once FeO becomes the majority oxide phase and at temperatures above 550 K, the interdiffusion between Pt and Fe atoms from Pt-rich FePt and Fe_3O_4/FeO components, respectively, begins and nucleates the Fe_3Pt compound. The amount of nucleated Fe_3Pt phase remains almost unchanged up to about 840 K, close to the temperature at which commonly the FePt soft to hard transformation occurs, where an abrupt increase of FeO percentage is observed. This second reduction step further drives the almost complete phase transformation to stabilize the Fe_3Pt phase. Magnetically, the postannealed sample shows soft properties with a high saturation magnetization. These results show that the reduction of magnetite and the emergence of wüstite as intermediate phase act as a catalyst that facilitates Fe and Pt interdiffusion to form Fe_3Pt instead of exchange coupled FePt/Fe_3Pt.[57] The interdiffusion is also helped by the fact that the metallic and oxide domains are continuously joined.

We conclude that inhibition of the Fe and Pt interdiffusion through the control of reducing mechanisms and interface influence should be of critical importance to synthesize tunable exchange-coupled materials for specific purposes. On the other hand, applications in the biomedicine field (drug delivery, hyperthermic ablation, or MRI) would require noncorrosive superparamagnetic materials with a large magnetization at rt. Under these requirements, annealed Pt-rich FePt/Fe_3O_4 heterodimer could be a promising candidate for these applications due to its larger magnetization in comparison with iron oxides, low corrosivity, and large stability, provided the coalescence and grain growth can be adequately controlled.

ASSOCIATED CONTENT

Supporting Information. Additional data about the EXAFS data analysis, experimental EXAFS characterization at the Pt L_3 edge of as-made sample, the factor analysis performed on the Fe K edge XANES, and the mass spectroscopy results are available. This information is available free of charge via the Internet at http://pubs.acs.org.

AUTHOR INFORMATION

Corresponding Author

*E-mail: pm.presa@pdi.ucm.es.

ACKNOWLEDGMENT

We appreciate financial support by LNLS, Campinas, SP, Brazil (proposals D06A−DXAS−7739 and D06A−DAXS−6669) and CONICET, Argentina. This work was supported by grants from the Spanish Ministry of Science and Innovation (CSD2007-00010, MAT2009-14741-C02-00) and the Madrid regional government CM (S009/MAT-1726). S.J.A.F. thanks M. Fernández-García and S. Pascarelli for fruitful comments on the manuscript. We thank F. Zambello (LNLS) and E. J. de Carvalho (LNLS) for their kind assistance during the DXAS experiments and G. Azevedo, C. Rodríguez Torres, and M. Ceolín for the beam time provided to perform the EXAFS experiments. P.P. thanks M. P. Morales for TEM images and ICP characterizations.

REFERENCES

(1) Zeng, H.; Sun, S. H. *Adv. Funct. Mater.* **2008**, *18*, 391.

(2) Carbone, L.; Cozzoli, P. D. *Nano Today* **2010**, *5*, 449.

(3) Song, H. M.; Wei, Q. S.; Ong, Q. K.; Wei, A. *ACS Nano* **2010**, *4*, 5163.

(4) de la Presa, P.; Multigner, M.; Morales, M. P.; Rueda, T.; Fernandez-Pinel, E.; Hernando, A. *J. Magn. Magn. Mater.* **2007**, *316*, E753.

(5) Yano, K.; Nandwana, V.; Chaubey, G. S.; Poudyal, N.; Kang, S.; Arami, H.; Griffis, J.; Liu, J. P. *J. Phys. Chem. C* **2009**, *113*, 13088.

(6) Wang, L. Y.; Luo, J.; Maye, M. M.; Fan, Q.; Qiang, R. D.; Engelhard, M. H.; Wang, C. M.; Lin, Y. H.; Zhong, C. J. *J. Mater. Chem.* **2005**, *15*, 1821.

(7) Garza-Navarro, M.; Torres-Castro, A.; Gonzalez, V.; Ortiz, U.; De la Rosa, E. *J. Solid State Chem.* **2010**, *183*, 99.

(8) Hartling, T.; Uhlig, T.; Seidenstucker, A.; Bigall, N. C.; Olk, P.; Wiedwald, U.; Han, L.; Eychmuller, A.; Plettl, A.; Ziemann, P.; Eng, L. M. *Appl. Phys. Lett.* **2010**, *96*, 183111.

(9) Gao, J. H.; Liang, G. L.; Zhang, B.; Kuang, Y.; Zhang, X. X.; Xu, B. *J. Am. Chem. Soc.* **2007**, *129*, 1428.

(10) Yin, Y. D.; Rioux, R. M.; Erdonmez, C. K.; Hughes, S.; Somorjai, G. A.; Alivisatos, A. P. *Science* **2004**, *304*, 711.

(11) Schartl, W. *Nanoscale* **2010**, *2*, 829.

(12) Yu, H.; Chen, M.; Rice, P. M.; Wang, S. X.; White, R. L.; Sun, S. H. *Nano Lett.* **2005**, *5*, 379.

(13) Figuerola, A.; Fiore, A.; Di Corato, R.; Falqui, A.; Giannini, C.; Micotti, E.; Lascialfari, A.; Corti, M.; Cingolani, R.; Pellegrino, T.; Cozzoli, P. D.; Manna, L. *J. Am. Chem. Soc.* **2008**, *130*, 1477.

(14) Wang, C.; Yin, H. F.; Dai, S.; Sun, S. H. *Chem. Mater.* **2010**, *22*, 3277.

(15) Casavola, M.; Falqui, A.; Garcia, M. A.; Garcia-Hernandez, M.; Giannini, C.; Cingolani, R.; Cozzoli, P. D. *Nano Lett.* **2009**, *9*, 366.

(16) Nandwana, V.; Chaubey, G. S.; Yano, K.; Rong, C. B.; Liu, J. P. *J. Appl. Phys.* **2009**, 105.

(17) Chen, S.; Wang, L. J.; Duce, S. L.; Brown, S.; Lee, S.; Melzer, A.; Cuschieri, S. A.; Andre, P. *J. Am. Chem. Soc.* **2010**, *132*, 15022.

(18) Gu, H. W.; Yang, Z. M.; Gao, J. H.; Chang, C. K.; Xu, B. *J. Am. Chem. Soc.* **2005**, *127*, 34.

(19) de la Presa, P.; Rueda, T.; Morales, M. P.; Hernando, A. *IEEE Trans Magn.* **2008**, *44*, 2816.

(20) Gu, H. W.; Ho, P. L.; Tsang, K. W. T.; Wang, L.; Xu, B. *J. Am. Chem. Soc.* **2003**, *125*, 15702.

(21) Maenosono, S.; Saita, S. *IEEE Trans. Magn.* **2006**, *42*, 1638.

(22) Morales, M. P.; Bedard, M. F.; Roca, A. G.; de la Presa, P.; Hernando, A.; Zhang, F.; Zanella, M.; Zahoor, A. A.; Sukhorukov, G. B.; del Mercato, L. L.; Parak, W. J. *J. Mater. Chem.* **2009**, *19*, 6381.

(23) Zeng, H.; Li, J.; Liu, J. P.; Wang, Z. L.; Sun, S. H. *Nature* **2002**, *420*, 395.

(24) Bodnarchuk, M. I.; Kovalenko, M. V.; Groiss, H.; Resel, R.; Reissner, M.; Hesser, G.; Lechner, R. T.; Steiner, W.; Schaffler, F.; Heiss, W. *Small* **2009**, *5*, 2247.

(25) Li, J.; Wang, Z. L.; Zeng, H.; Sun, S. H.; Liu, J. P. *Appl. Phys. Lett.* **2003**, *82*, 3743.

(26) Hernando, A.; Navarro, I.; Gonzalez, J. M. *Europhys. Lett.* **1992**, *20*, 175.

(27) Arcas, J.; Hernando, A.; Barandiaran, J. M.; Prados, C.; Vazquez, M.; Marin, P.; Neuweiler, A. *Phys. Rev. B* **1998**, *58*, 5193.

(28) Poudyal, N.; Chaubey, G. S.; Rong, C. B.; Liu, J. P. *J. Appl. Phys.* **2009**, *105*, 07A749.

(29) Nandwana, V.; Chaubey, G. S.; Yano, K.; Rong, C. B.; Liu, J. P. *J. Appl. Phys.* **2009**, *105*, 014303.

(30) Wilke, M.; Farges, F.; Petit, P. E.; Brown, G. E.; Martin, F. *Am. Mineral.* **2001**, *86*, 714.

(31) Tolentino, H. C. N.; Cezar, J. C.; Watanabe, N.; Piamonteze, C.; Souza-Neto, N. M.; Tamura, E.; Ramos, A.; Neueschwander, R. *Phys. Scr.* **2005**, *T115*, 977.

(32) Fernandez-Garcia, M. *Catal. Rev.-Sci. Eng.* **2002**, *44*, 59.

(33) Fernandez-Garcia, M.; Alvarez, C. M.; Haller, G. L. *J. Phys. Chem.* **1995**, *99*, 12565.

(34) Figueroa, S. J. A.; Stewart, S. J. *J. Synchrotron Radiat.* **2009**, *16*, 63.

(35) Marquez-Alvarez, C.; Rodriguez-Ramos, I.; Guerrero-Ruiz, A.; Haller, G. L.; Fernandez-Garcia, M. *J. Am. Chem. Soc.* **1997**, *119*, 2905.

(36) Lagarec, K.; Rancourt, D. G.; *Recoil, Version 1.0*; Department of Physics, University of Ottawa: Ottawa, Canada, 1998.

(37) Corrias, A.; Mountjoy, G.; Loche, D.; Puntes, V.; Falqui, A.; Zanella, M.; Parak, W. J.; Casula, M. F. *J. Phys. Chem. C* **2009**, *113*, 18667.

(38) de la Presa, P.; Rueda, T.; Hernando, A.; Ramallo-Lopez, J. M.; Giovanetti, L. J.; Requejo, F. G. *J. Appl. Phys.* **2008**, *103*, 103909.

(39) Wang, H. L.; Huang, Y.; Zhang, Y.; Hadjipanayis, G. C.; Weller, D.; Simopoulos, A. *J. Magn. Magn. Mater.* **2007**, *310*, 22.

(40) Stahl, B.; Ellrich, J.; Theissmann, R.; Ghafari, M.; Bhattacharya, S.; Hahn, H.; Gajbhiye, N. S.; Kramer, D.; Viswanath, R. N.; Weissmuller, J.; Gleiter, H. *Phys. Rev. B* **2003**, *67*, 014422.

(41) Delalande, M.; Marcoux, P. R.; Reiss, P.; Samson, Y. *J. Mater. Chem.* **2007**, *17*, 1579.

(42) Goya, G. F.; Berquo, T. S.; Fonseca, F. C.; Morales, M. P. *J. Appl. Phys.* **2003**, *94*, 3520.

(43) Vandenberghe, R. E.; Nedkov, I.; Merodiiska, T.; Slavov, L. *Hyperfine Interact.* **2005**, *165*, 267.

(44) Cozzoli, P. D.; Snoeck, E.; Garcia, M. A.; Giannini, C.; Guagliardi, A.; Cervellino, A.; Gozzo, F.; Hernando, A.; Achterhold, K.; Ciobanu, N.; Parak, F. G.; Cingolani, R.; Manna, L. *Nano Lett.* **2006**, *6*, 1966.

(45) Buonsanti, R.; Grillo, V.; Carlino, E.; Giannini, C.; Curri, M. L.; Innocenti, C.; Sangregorio, C.; Achterhold, K.; Parak, F. G.; Agostiano, A.; Cozzoli, P. D. *J. Am. Chem. Soc.* **2006**, *128*, 16933.

(46) Roca, A. G.; Marco, J. F.; Morales, M. D.; Serna, C. J. *J. Phys. Chem. C* **2007**, *111*, 18577.

(47) Daou, T. J.; Greneche, J. M.; Lee, S. J.; Lee, S.; Lefevre, C.; Begin-Colin, S.; Pourroy, G. *J. Phys. Chem. C* **2010**, *114*, 8794.

(48) Yoshida, H.; Nonoyama, S.; Yazawa, Y.; Hattori, T. *Phys. Scr.* **2005**, *T115*, 813.

(49) Bazin, D.; Sayers, D.; Rehr, J. J.; Mottet, C. *J. Phys. Chem. B* **1997**, *101*, 5332.

(50) Ciuparu, D.; Haider, P.; Fernandez-Garcia, M.; Chen, Y.; Lim, S.; Haller, G. L.; Pfefferle, L. *J. Phys. Chem. B* **2005**, *109*, 16332.

(51) Oneill, H. S. *Am. Mineral.* **1988**, *73*, 470.

(52) Sun, S. H.; Murray, C. B.; Weller, D.; Folks, L.; Moser, A. *Science* **2000**, *287*, 1989.

(53) Lyubina, J. *Nanocrystalline Fe-Pt Alloys: Phase Transformations, Structure and Magnetism*; Cuvillier Verlag: Dresden, 2007.

(54) Lai, F. J.; Chou, H. L.; Sarma, L. S.; Wang, D. Y.; Lin, Y. C.; Lee, J. F.; Hwang, B. J.; Chen, C. C. *Nanoscale* **2010**, *2*, 573.

(55) Buschow, K. H. J.; Vanengen, P. G.; Jongebreur, R. *J. Magn. Magn. Mater.* **1983**, *38*, 1.

(56) Baldokhin, Y. V.; Kolotyrkin, P. Y.; Petrov, Y. I.; Shafranovsky, E. A. *J. Appl. Phys.* **1997**, *82*, 3042.

(57) Rong, C. B.; Nandwana, V.; Poudyal, N.; Li, Y.; Liu, J. P.; Ding, Y.; Wang, Z. L. *J. Phys. D: Appl. Phys.* **2007**, *40*, 712.